Received: 21 December 2022 | Revised: 18 March 2023 | Accepted: 4 April 2023

DOI: 10.1002/esp.5599

RESEARCH ARTICLE

ESPL WILEY

Controls of local grain size distribution, bed structure and flow conditions on sediment mobility

Heidi E. J. Smith[1] | Angel D. Monsalve[2,3] | Jens M. Turowski[4] | Dieter Rickenmann[5] | Elowyn M. Yager[3]

[1]Center for Ecohydraulics Research, Department of Water Resources, University of Idaho, Boise, Idaho, USA

[2]Departamento de Ingenieria de Obras Civiles, Universidad de la Frontera, Temuco, Chile

[3]Center for Ecohydraulics Research, Department of Civil and Environmental Engineering, University of Idaho, Boise, Idaho, USA

[4]German Research Centre for Geosciences GFZ, Helmholtzzentrum Potsdam, Potsdam, Germany

[5]Swiss Federal Research Institute WSL, Mountain Hydrology and Torrents, Birmensdorf, Switzerland

Correspondence
Heidi E. J. Smith, Center for Ecohydraulics Research, Department of Water Resources, University of Idaho, Boise, Idaho, USA.
Email: heidismith@uidaho.edu

Funding information
National Science Foundation, Grant/Award Number: 0847799

Abstract

Steep, boulder bed streams often contain sediment patches, which are areas of the bed with relatively well-defined boundaries that are occupied by distinct grain size distributions (GSD). In sediment mixtures, the underlying GSD affects the critical Shields stress for a given grain size, which is commonly predicted using hiding functions. Hiding functions may vary with reach-wide bed GSD, but the effect of local GSD on relative sediment mobility between sediment patches is poorly understood. We explore the effects of patch-scale GSD on sediment mobility using tracer particles combined with local shear stresses to develop hiding functions for different patch classes within a steep stream. Hiding functions for all tested patch classes were similar, which indicates that the same hiding function can be used for different patches. However, the critical Shields stress for a given grain size generally decreased with lower patch median grain size (D_{50}) suggesting that patches control the relative mobility of each size through both the underlying GSD and local shear stresses. The effects of the underlying GSD partly depend on grain protrusion, which we measured for all grain sizes present on each patch class. Protrusion was generally greater for larger grains regardless of patch class, but for a given grain size, protrusion was increased with smaller patch D_{50}. For a given grain size, higher protrusion results in greater applied fluid forces and reduced resisting forces to partly explain our lower critical Shields stresses in finer patches. Patches therefore can importantly modulate relative sediment mobility through bed structure and may need to be included in reach-scale sediment transport and channel stability estimates.

KEYWORDS
critical Shields stress, grain size distribution, hiding effects, local grain protrusion, relative grain size, spatial distribution of shear stresses, textural patches

1 | INTRODUCTION

The success of river restoration and instream construction (e.g., bridges and channel bank reinforcements) projects rely on accurate estimates of the flows that initiate sediment motion (Malakoff, 2004; Palmer et al., 2005; Skidmore et al., 2001). However, orders of magnitude errors often exist in predicted bedr transport rates in steep (gradient >3%), boulder bed streams (Bathurst, 1987; D'Agostino & Lenzi, 1999; Rickenmann, 1997). These errors partly stem from the difficulty in accurately determining the onset of sediment motion (Beheshti & Ataie-Ashtiani, 2008; Diplas et al., 2008; Houssais et al., 2015; Lee & Balachandar, 2012; Wiberg & Smith, 1987). The onset of particle motion is typically represented by the dimensionless reach-averaged shear stress $\left(\tau^*_{c_i}\right)$ needed to move a certain grain size (D_i) (Beheshti & Ataie-Ashtiani, 2008; Diplas et al., 2008; Houssais et al., 2015; Lee & Balachandar, 2012; Shields, 1936; Wiberg & Smith, 1987):

$$\tau^*_{c_i} = \frac{\tau_{c_i}}{(\rho_s - \rho_w) g D_i} \quad (1)$$

where τ_{c_i} is the critical shear stress required to move D_i, g is acceleration due to gravity and ρ_s and ρ_w are the densities of sediment and

water, respectively. For heterogeneous mixtures of sediment, the critical Shields stress for a given grain size often varies with D_i and the underlying median grain size (D_{50}). The relative mobility of each grain size can be calculated with hiding functions, which have the form:

$$\tau^*_{c_i} = \tau^*_{c_{50}} \left(\frac{D_i}{D_{50}} \right)^{-\gamma} \quad (2)$$

where γ and $\tau^*_{c_{50}}$ are empirically fit values for the hiding function exponent and the critical Shields stress for the D_{50}, respectively.

Hiding functions indirectly represent the fact that small grains are often hidden from the flow within the matrix of the bed material, whereas larger grains can extend higher in the flow. Hiding functions also indirectly incorporate the fact that the mobility of a given grain size depends on the grain size distribution of the underlying bed, which can shelter or expose surface grains. Thus, small grains within a wide mix of grain sizes can have higher critical Shields stresses than estimated with their weight alone, whereas coarser grains can become more mobile relative to their weight. The exponent of the hiding function could range in theory between −1 (all grain sizes move at the same Shields stress; hiding effects counteract weight effects) and 0 (only weight effects control motion).

Hiding functions can vary widely between different streams (e.g., Buffington & Montgomery, 1999) and this is partly because these equations are typically developed using reach-averaged shear stresses, reach-averaged D_{50} and reach-averaged D_i mobility. The onset of sediment motion instead occurs at the particle scale when the stabilizing force that is a function of grain weight, intergranular friction, protrusion (vertical distance a grain extends above surrounding bed sediment) and pivot angle (the angle through which a grain must pivot) is exceeded by the driving forces of drag and lift (Schmeeckle et al., 2007; Wiberg & Smith, 1987; Yager et al., 2018), which are influenced by protrusion and local flow conditions. In natural stream beds, the heterogeneous arrangement of sediment creates a distribution of possible surface positions for each grain size, which influences pivot angles, intergranular friction, and protrusion. Different particle positions relative to the thalweg or to flow obstructions can also influence the local flow field and drag and lift forces. Larger pivot angles have been associated with greater resisting forces that impede grain motion (Buffington et al., 1992; Hodge et al., 2013; Kirchner et al., 1990; Prancevic & Lamb, 2015). However, recent evidence suggests that pivot angle could have a negligible influence on sediment entrainment compared to other variables (Hodge et al., 2020). Intergranular friction incorporates the effects of particle interlocking, particle arrangement, bed compaction and dilation, and bed porosity and increases particle resistance to motion (e.g., Cúñez et al., 2022; Hodge et al., 2013; Yager et al., 2018). While decreasing grain burial and therefore bed resisting forces (Yager et al., 2018), greater protrusion can increase drag forces and decrease lift forces (Schmeeckle et al., 2007). The net result is that grains typically become easier to move as their protrusion increases (Buffington et al., 1992; Hodge et al., 2020; Hodge et al., 2013; Kirchner et al., 1990; Masteller & Finnegan, 2017; Voepel et al., 2019; Yager et al., 2018).

In particular, protrusion has been identified in many studies as a key control on particle mobility and is therefore a strong potential influence on the hiding function exponent. Larger grain sizes may feature larger protrusions than smaller grains (e.g., Kirchner et al., 1990), which is often used to indirectly explain hiding effects. The underlying bed grain size distribution (GSD) could also influence protrusion through the creation of different sized pockets or grain burial, which could control the strength of hiding effects. Therefore, variations in protrusion between rivers may partly explain the wide range of observed hiding functions. Concurrent measurements of particle protrusion and the onset of sediment transport, which is needed to construct hiding functions, have not occurred to test the importance of protrusion in controlling both the occurrence of hiding effects and the strength of these effects.

Some of the variability in hiding functions is also likely because of spatial variations in GSD and flow hydraulics within a given river, which are particularly pronounced in steep mountain streams (Monsalve et al., 2016; Yager et al., 2012a). Grains are often organized into patches, where the borders of each patch can be visually defined by a distinct change in GSD, indicating a delineation between patches (Buffington & Montgomery, 1999; Dietrich et al., 2005; Monsalve et al., 2016; Yager et al., 2012a). Some studies have shown that the relative mobility of a given grain size changes with patch GSD; small grains may preferentially move from fine patches compared to coarse patches (Lisle, 1995; Vericat et al., 2008). This change in the mobility of a given grain size could be driven by patch GSD effects on grain protrusion as well as the flow conditions that are dictated by each patch. For example, small grains on fine patches could have high protrusions, whereas on coarse patches, small grains may have low protrusions and be more difficult to move. However, in other studies, a given grain size moved at the same flow magnitude for all underlying patch GSD (Dietrich et al., 2005; Yager et al., 2012b), suggesting that local protrusion and flow hydraulics do not affect sediment motion. For example, coarser patches could systematically be subjected to higher near-bed stresses than fine patches thereby possibly increasing local grain mobility (Monsalve et al., 2016). Therefore, the control of local GSD on protrusion and the influence of both local GSD and shear stresses on hiding functions is currently not known.

Finally, these uncertainties about local GSD effects on protrusion and hiding functions cannot be addressed without accurate measurements or predictions of protrusion. No generally applicable predictive relation exists to calculate protrusion and no universal definition of protrusion exists. Protrusion (or similar terms, projection and exposure) has been defined as the grain height relative to the elevation of the immediate upstream grain (Wiberg & Smith, 1987) or the difference between the maximum height of a particle of interest and the height of surrounding grains a distance D_{84} around the grain (Hodge et al., 2013; Kirchner et al., 1990). The relative elevations of grains farther upstream of the neighbouring particle may still cause sheltering for the particle of interest but the distance over which protrusion needs to be calculated is not currently known.

To address these key uncertainties about protrusion, we focus on determining: (i) the influence of upstream measurement distance on protrusion, (ii) the influence of patch GSD on protrusion of a given grain size and (iii) a general equation to estimate protrusion using the underlying patch GSD. We measured grain protrusions at multiple spatial scales on different patch classes in a steep, step-pool channel to answer these questions. To understand how the relative mobility of

a given grain size varies with patch GSD, we measured tracer grain motion (painted, numbered and tagged rocks placed on the stream bed) from the same patch classes as those used for the protrusion measurements. We then developed hiding functions for each patch class and all patch classes combined using tracer particle motions and patch-scale shear stresses, which were estimated with a quasi-3D model (Monsalve et al., 2016). Finally, we compared these hiding functions between patch classes to determine the: (i) variation of hiding functions between patch classes, (ii) role of shear stress uncertainty in controlling hiding functions, (iii) influence of patch GSD on the critical shear stress for a given grain size and (iv) the potential role of protrusion in controlling these hiding functions.

2 | METHODS AND MATERIALS

2.1 | Study site

We conducted field work (June to August of 2011) in the Erlenbach (Brunni, Switzerland), which is managed by the Swiss Federal Institute for Forest, Snow and Landscape Research (WSL) and is characterized by frequent sediment-transport events. This field site has been described in depth with a detailed site map in previous studies (e.g., Beer et al., 2015; Burtin et al., 2016; Masteller et al., 2018; Nitsche et al., 2011; Rickenmann, 1997; Rickenmann et al., 2012; Rickenmann & McArdell, 2007; Schneider et al., 2015; Turowski et al., 2009; Wyss et al., 2016; Yager et al., 2012, 2012a, 2012b), and we only focus on the relevant details for this study. The runoff regime in the Erlenbach catchment is nivo-pluvial with peak discharges caused by intense flash floods during the summer (Molnar et al., 2010; Schneider et al., 2015). The WSL measures discharge every 10 minutes at the downstream boundary of our reach (Beer et al., 2015; Rickenmann & McArdell, 2007) and sediment transport has been recorded during storm events with discharges between 0.1 and 12 m^3/s (Rickenmann et al., 2012; Turowski et al., 2009). Our study reach is 50 m long, 4.7 m wide, steep (10% reach-averaged bed slope), has a bankfull discharge of 1.7 m^3/s (Nitsche et al., 2012) and is characterized by boulder steps that remain emergent at lower flow events, become fully submerged at higher discharges, and rearranged at discharges between 7 and 10 m^3/s (Turowski et al., 2013) that occur infrequently (≥25 years).

2.2 | Defining patches

To characterize the spatial variability of grain size distributions within our reach we created a sediment patch map following the methods outlined by Yager et al. (2012a) and Monsalve et al. (2016). In the field each patch was visually delimited by identifying a clear change in surface texture and characterized by the dominant surface grain size class (e.g., sand (<2 mm), gravel (2–63 mm), cobble (64–256 mm) and boulder (>256 mm)) according to the classification method of Buffington & Montgomery (1999). If at least 5% of the patch surface was occupied by one or more size classes, a subdominant grain size class amended the name (e.g., gC classification: dominant cobble, subdominant gravel). During data processing we amended the patch classification (7% of all patches) if the pebble count indicated a different grain size classification than what we had estimated visually (e.g., cG became a gC). We identified a total of six patch classes distributed into 62 individual patches. The final patch map and GSD for each patch class can be found in Monsalve et al. (2016) and a detailed patch map can also be found in the supporting information.

2.3 | Grain size distributions

To characterize the GSD for each patch class we conducted pebble counts on multiple patches within each patch class until a representative sample was collected (Wolman, 1954). The total number of grains measured on each patch class were: 121 grains on two patches (G), 121 grains on three patches (cG) and 123 grains on three patches (gC). We used a grid to sample grains with the spacing being greater than the largest grain size on the patch to avoid resampling large grains. Grain sizes were measured in half-phi intervals using a gravelometer. Further details on the pebble counts can be found in Monsalve et al. (2016).

2.4 | Tracer grains

We monitored tracer grain movements after 9 transport events in 2011 (Table 1), of which a subset of these storm events was used to predict local shear stresses by Monsalve et al. (2016). Rocks for tracer grains were collected immediately upstream of our study reach to avoid disturbing our site and were sorted into half phi size classes (11 to 128 mm) using a gravelometer. Grains 32 mm and larger were implanted with a radio-frequency identification (RFID) tag, which was placed into a cavity made with a drill press and fixed in place using epoxy (Lamarre et al., 2005; Schneider et al., 2014). Then, each grain size class was painted a unique colour and each individual grain was uniquely identified by a written number on the grain surface. Grains smaller than 32 mm were also painted based on their half phi size class, and then identified uniquely with a written number on the grain surface. The primary three axes and weights were measured for all tracers.

To optimally characterize the most common patch classes of the potentially mobile portion of the bed (Monsalve et al., 2016; Yager et al., 2012a), we populated cobble-Gravel (cG), gravel-Cobble (gC), and Gravel (G) patches (28%, 17%, and 14% of total bed area respectively) with tracer particles. We matched the installed tracer size distribution to that of each underlying patch such that the original patch class GSD was not altered. We placed a relatively small amount of tracer grains, approximately 20 tracers/m^2 of bed surface to avoid overpopulating a certain patch (Table 1). With the dual purpose of placing tracer grains in natural positions and avoiding changing the patch GSD, we removed in-situ grains in random locations and replaced them with tracers in the same approximate position and orientation. Hereinafter, we refer to these patches with matching tracer and patch GSD as fully populated patches. Tracers were installed in fully populated patches at the beginning of the summer season and mobilized tracers out of these patches were periodically replaced with new particles between storm events to ensure a sufficient sample size for all events.

TABLE 1 Mobile D_{84} used in hiding functions and the number of grains (n) used to calculate the mobile D_{84} during each peak discharge (Q_p) for each patch class (G, cG and gC). The maximum grain size (D_{max}) present for each patch class and the number of installed grains (n) is indicated. To contextualize the flows that we measured, the magnitude of the bankfull discharge is 1.7 m^3/s.

			Mobile grains		Installed grains	
Date	Patch class	Q_p (m^3/s)	D_{84} (mm)	n	D_{max} (mm)	n
4-Aug	G	0.173	16	1	128	45
8-Jul	G	0.273	23	1	128	89
10-Aug	G	0.522	22	4	128	47
17-Jul	G	0.600	21	2	128	47
24-Jul	G	0.611	NA	0	128	41
20-Jul	G	0.690	27	4	128	44
13-Jul	G	0.838	11	1	128	46
7-Aug	G	0.888	78	4	128	44
10-Jul	G	0.890	45	15	128	54
30-Jun	G	2.103	50	18	128	40
4-Aug	cG	0.173	16	7	256	44
8-Jul	cG	0.273	87	5	256	88
10-Aug	cG	0.522	64	13	256	33
17-Jul	cG	0.600	110	4	256	38
24-Jul	cG	0.611	45	1	256	31
20-Jul	cG	0.690	16	20	256	49
13-Jul	cG	0.838	74	11	256	68
7-Aug	cG	0.888	90	27	256	35
10-Jul	cG	0.890	90	17	256	48
30-Jun	cG	2.103	74	11	256	21
4-Aug	gC	0.173	16	10	364	46
8-Jul	gC	0.273	64	15	364	129
10-Aug	gC	0.522	38	23	364	50
17-Jul	gC	0.600	90	6	364	53
24-Jul	gC	0.611	104	5	364	36
20-Jul	gC	0.690	64	29	364	52
13-Jul	gC	0.838	90	20	364	56
7-Aug	gC	0.888	90	24	364	47
10-Jul	gC	0.890	90	36	364	76
30-Jun	gC	2.103	64	43	364	59

Fully populated patches were not always submerged during lower flow events that could transport sediment. We therefore also placed large tracer sizes (90 and 128 mm) in cG, gC and C (5% of total bed area) patches that were always submerged to ensure that we observed entrainment of large grains. These patches were not populated with a full distribution of grain sizes and are hereafter defined as submerged patches. When tracers moved out of the fully populated patches, they often deposited on continually submerged patches. Tracers also were fluvially re-located to other patch classes on which we had not installed any tracers: Boulder, boulder-Cobble, and boulder-gravel-Cobble (26%, 8% and 2% of total bed, respectively).

The placed tracers were likely less stable than in-situ grains, which would cause tracer grains to move at lower peak discharges than naturally deposited grains (Schneider et al., 2014). However, the first mobilization of tracer grains has been previously used in published studies (e.g., Olinde & Johnson, 2015). We included the first tracer motions to (1) treat all tracers consistently between the patch classes (gC, cG, G) of interest and (2) avoid having a low sample size of mobile grains and storm events. In general, our tracer recovery rate for all grain size classes after all storm events ranged from 35%–92% and averaged 76%, which is in the range of typical recovery rates (e.g., Lamarre et al., 2005; Olinde & Johnson, 2015). The lowest recovery rate was due to a large storm event that either buried or transported tracers out of the study reach into a sediment retention basin that is immediately downstream of the reach.

The methods we used to record tracer locations were (1) a total station survey, (2) the horizontal distances of the tracers from three local surveyed and spray-painted fixed points and (3) photographs taken parallel to the bed (plan view) using a camera fixed to a level-mounted pole, to visualize both tracer grains and surveyed fixed points. Although the total station was the most accurate method and was used as much as possible (three surveys measuring 287 grain locations season-wide), we often relied on methods 2 and 3 because they were readily available immediately after storm events and faster to document all tracer positions before the next immediately incoming storm event. Storm events lasted a few hours to multiple days and some events occurred in quick succession (see Table 1). The discharge between all events declined below that needed to mobilize tracer particles and allowed us to visually see the bed and the particles. Coordinates for tracers using method 2 were identified by defining a circle centred on each surveyed fixed point with the radius set by the measured distance to the tracer. Then, we found the area of overlap for the three circles and the tracer coordinates were at the centroid of this overlapping area. Tracer coordinates were found using method 3 by overlapping the photographs with a grid of coordinates where two or more surveyed fixed points were located. This process scaled and oriented the photographs within the fixed-point coordinate system, such that the coordinates of each tracer could be identified.

Using these known tracer coordinates (methods 1–3) before and after each event we determined that a tracer moved in a storm event when its calculated transport distance was greater than the largest error associated with all three methods. The largest error was estimated by comparing the locations of a set of tracer grains calculated using method 2 (17 grains) and method 3 (4 grains) to those also measured with the total station. The errors associated with methods 2 and 3 were separately calculated by finding for each tracer location the distance between the estimated and total station coordinates. For each method, using the distribution of error distances from all tested tracers we calculated the root-mean-square error (RMSE, method 2 = 0.1604 m and 3 = 0.1598 m). Based on Yager et al. (2012a), two times the RMSE resulted in a 95% confidence interval for tracer grain locations, which would equal 0.32 m. Given that method 3 only had 4 comparison tracers, we used a more conservative threshold of 0.5 m to define the minimum distance needed for tracer movement. Thus, when a tracer grain had moved more than 0.5 m, the peak discharge that occurred prior to finding the grain was assumed to be the discharge responsible for motion.

As is common practice in tracer particle studies, tracer movements were assumed to be associated with the peak discharge of the event that preceded their displacement because tracer movements could not be surveyed during high flow events. Oftentimes, the smallest grains (less than 22.6 cm) were permanently lost in the flow event that occurred immediately after their placement. In this circumstance, we assumed that the tracer grain moved during the peak discharge that occurred between the dates when it was placed and subsequently lost. If a tracer grain larger than 32 mm in diameter was permanently lost, it was assumed to have moved if the repeat photographs provided evidence that the grain was not buried in its original location (e.g., buried and then uncovered in the same location), and the event just prior to losing the grain was considered to have caused its motion.

2.5 | Protrusion measurements

We measured protrusions (P) for each half phi grain size class (including tracers and in-place grains) present in G, cG and gC patches. We used a custom built portable device that unobtrusively measured elevations from a set horizontal datum for the grain of interest and for upstream locations at a spacing of 1 cm. This device used thin plastic strips (1 cm wide × 30 cm tall) that were clamped together between two horizontal blocks fixed to a level. Positioned adjacent to one another, each strip independently and vertically shifted to measure a 48-cm-long transect of elevations. Test transects taken at horizontal angles of 45° from the upstream direction and transects taken in a direction immediately upstream from the grain of interest were similar. Thus, we collected upstream protrusion transects only, which were parallel to the overall channel direction. For each half phi grain size class and patch class combination, we collected transects for multiple grains to include a range of grain placements (Table 2). We collected a variable number of protrusion transects with patch coarseness, with a larger sample size for coarser patches to capture the greater variability of elevations present than on finer patches. For each transect, we calculated (a) an immediate upstream grain protrusion by using the difference in elevation between each grain of interest and the immediate upstream bed elevation, which is 1 cm away from the particle or closer and (b) an extended upstream grain protrusion that used the difference between the grain of interest elevation and the median of the elevations measured up to 48 cm upstream. We calculated the median protrusion using each method for each grain size class and patch class combination. Thus, hereafter, the median protrusion generally refers to the median for each grain size class and patch class combination rather than the protrusion calculated for a given transect, and specifically median immediate protrusion and median extended protrusion are denoted as P_i and P_e, respectively. However, we also tested the influence of incrementally adding more upstream elevation measurements in the calculation of a median protrusion for each transect. For all methods, negative protrusions represent grains of interest that were below the elevation of the surrounding upstream bed, and positive protrusions were grains that were higher in elevation than the surrounding bed.

TABLE 2 Number of protrusion transects collected for each grain size class and patch class combination.

	Patch class		
Surface grain size (mm)	G	cG	gC
11	9	11	19
16	4	17	21
22.6	5	16	28
32	4	15	27
45	4	18	37
64	11	18	44
90	11	19	50
128	4	19	31

2.6 | Modelling shear stresses during peak flow events

We used local shear stresses for each patch class, rather than assuming a reach-averaged shear stress that is often used in hiding functions, because local shear stress distributions vary with patch class (Monsalve et al., 2016). We used the quasi-3D hydrodynamic model, FaSTMECH (Flow and Sediment Transport and Morphological Evolution of Channels, McDonald et al., 2005) to obtain the spatial distribution of shear stresses in the entire river reach. The model, developed by the US Geological Survey (USGS) and distributed by the International River Interface Cooperative (iRIC, www.i-ric.org), solves the vertically-averaged conservation of mass and Reynolds-averaged momentum equations in an orthogonal curvilinear coordinate system (Nelson & Smith, 1989). The depth-averaged solutions assume steady and hydrostatic flow. Turbulence effects are simplified assuming homogeneous and isotropic characteristics and modeled using a zero-equation model for the lateral eddy viscosity (Barton et al., 2005; Miller & Cluer, 1998; Nelson et al., 2003). Approximated vertical velocity profiles are based on the two-dimensional (2D) solutions and the turbulence closure model (Rattray & Mitsuda, 1974). FaSTMECH has been widely used in field studies (e.g., Clayton & Pitlick, 2007; Conner & Tonina, 2014; Maturana et al., 2014; Monsalve et al., 2016, 2020; Mueller & Pitlick, 2014; Nelson et al., 2010; Segura & Pitlick, 2015) and specific details of the model are given by Nelson and McDonald (1996).

We simulated the entire range of flows (0.20 to 2.1 m^3/s, increments of 0.05 m^3/s) that occurred while we tracked our tracer grains. We measured depths at five cross-sections throughout a range of flow events to calibrate the model. The model uses two parameters to calibrate a given flow discharge, the lateral eddy viscosity and the bed surface roughness. We set the lateral eddy viscosity to 0.005 m^2/s for all our simulated discharges and varied the bed surface roughness using a drag coefficient (C_d) to obtain a good agreement between observed and predicted flow depths. We analysed two different approaches for C_d in our simulations, a spatially variable or constant drag coefficient. A spatially constant C_d implies that the flow is relatively insensitive to local changes in roughness and responds slowly to variations in sediment size. A spatially variable C_d reflects sensitivity to local variations in grain size. For example, coarser patches will have a higher C_d resulting in slower velocities while finer patches will have a lower C_d resulting in higher velocities.

We computed the local shear stress (τ_n) directly in FaSTMECH at every node of our mesh (10 × 10 cm cell size). Estimates are based on the 2D velocity solutions according to

$$\tau_n = \rho C_d \left(u_n^2 + v_n^2\right) \quad (3)$$

where the subscript n indicates a given node, and u_n and v_n are the vertically averaged streamwise and cross-stream velocities, respectively. We analysed the sensitivity of our local shear stress estimates to the approach used to specify C_d. As previously shown by Monsalve et al. (2016) for the same reach of the Erlenbach the use of constant drag coefficient results in similar predictions of the patch averaged shear stresses compared to those determined using a spatially variable drag coefficient despite the apparent difference in the underlying assumptions. This occurs because there is a trade-off between the local drag coefficient and velocity values. Low or high C_d results in high or low local velocity, respectively, thus maintaining the value of τ_n in Equation (3). Our findings are consistent with those of Katz et al. (2018), Lisle et al. (2000), Nelson et al. (2010), and Segura & Pitlick (2015) supporting our choice of using a constant drag coefficient for all our simulated discharges. Using a spatially constant drag coefficient that inversely varied with discharge (C_d range of 0.12–0.26) provided the best model calibration results. Additional details on flow measurements, use of C_d, and model calibration can be found in Monsalve et al. (2016).

2.7 | Hiding functions

We developed a hiding function for each patch class (G, cG and gC) and for all three of these patch classes combined. Hiding functions require a critical Shields stress that is associated with the motion of a half phi interval grain size class (D_i). For each patch class and tracer moving flow event, we used FaSTMECH to obtain a spatial distribution of shear stresses for the peak discharge and then used the median shear stress for each patch class as the critical shear stress. Normally, this critical shear stress is associated with the maximum tracer size that moved in a certain flow event. Given uncertainties in the maximum mobile tracer size, we instead used the D_{84} of the mobile tracer grain size distribution (Table 1) for each patch class and transport event following Yager et al. (2012a). Errors in the mobile D_{84} may exist for some flow events and patch classes because of a small number of observed mobile tracer grains. Tracers moved from patches with a full grain size distribution of installed tracers, as well as from patches that had as few as a single tracer, which had been deposited during the previous storm event. We therefore produced two sets of hiding functions for each patch class using (i) the D_{84} of mobile tracers and median shear stresses on only fully populated patches that had mobile tracers in a given event and (ii) the D_{84} of mobile tracers and median shear stresses associated with any patches from which mobile tracers moved (includes fully populated and fully submerged patches, hereafter referred to as all mobile patches) in a given event. To calculate relative grain size, we used the D_{50} for each patch class hiding function, and the average D_{50} of all G, cG and gC patches (42 mm) for the combined patch class hiding function.

3 | RESULTS

3.1 | Protrusion variation with transect distance

We explored how including progressively longer transect lengths (2-cm increments, for a total length of 2 to 48 cm) affected the median protrusion of multiple transects for each D_i and patch class combination (Figure 1). For grains larger than the D_{50} of each patch class, the median protrusion estimates were generally constant regardless of the transect length; protrusions measured at locations nearest to the grain roughly equalled the median computed for the entire transect. In contrast, for grain sizes smaller than the patch D_{50}, as the transect length increased the median protrusion decreased in cG and gC patches and increased in G patches.

Protrusion-averaging transect length (immediate upstream (P_i) vs. extended upstream (P_e)) affected the median protrusion measured for each D_i and patch class combination (Figure 2). Three major differences between these two methods of defining protrusion occurred. First, for a given grain size, greater median protrusion differences between different patch classes generally occurred when using P_e compared to P_i. Second, for the smallest grains in cG and gC patches, P_i was near zero, whereas the P_e was negative. Third, P_i was the same for small grains (~ < 30 mm) on all patches whereas P_e for small grains decreased with patch D_{50}. Similarities between P_i and P_e were that (i) tracers protruded more as the grain size of interest increased, (ii) coarse grains had lower median protrusion with patch coarsening (D_{50} are G: 20 mm, cG: 50 mm; gC: 57 mm) and (iii) for G patches, the median protrusion was positive for all grain sizes.

3.2 | Protrusion variation with grain size and patch class

Regardless of protrusion definition, protrusion was higher with increasing grain size and was often smaller on coarse patches than finer patches (Figure 2) implying that both grain size and patch GSD affect protrusion. Given these effects, we calculated dimensionless grain sizes and protrusion to determine if a single relation between these variables and protrusion could be developed. The dimensionless grain size was D_i (from Figure 2) divided by the D_{50} of each patch class. Dimensionless protrusion was the measured protrusion for each grain divided by either its (1) grain size (i.e., b-axis) (Figure 3a,c) or (2) measured c-axis, which we assumed is the vertical grain axis when a grain sits on the bed (Figure 3b,d). The c-axis may better estimate protrusion and more accurately predict the onset of motion than the b-axis (Voepel et al., 2019). We then calculated the median dimensionless protrusion for a given patch class and dimensionless grain size bin using both P_e and P_i.

The median dimensionless protrusion increased with dimensionless grain size regardless of how dimensionless protrusion was calculated (i.e., using P_e vs. P_i, b- vs. c-axis). The highest R^2 of all possible dimensionless protrusion and D_i/D_{50} relations occurred for P_e when normalized with the c-axis. For all patch classes, the relations between dimensionless median protrusion and dimensionless grain size also generally collapsed on a single logarithmic line.

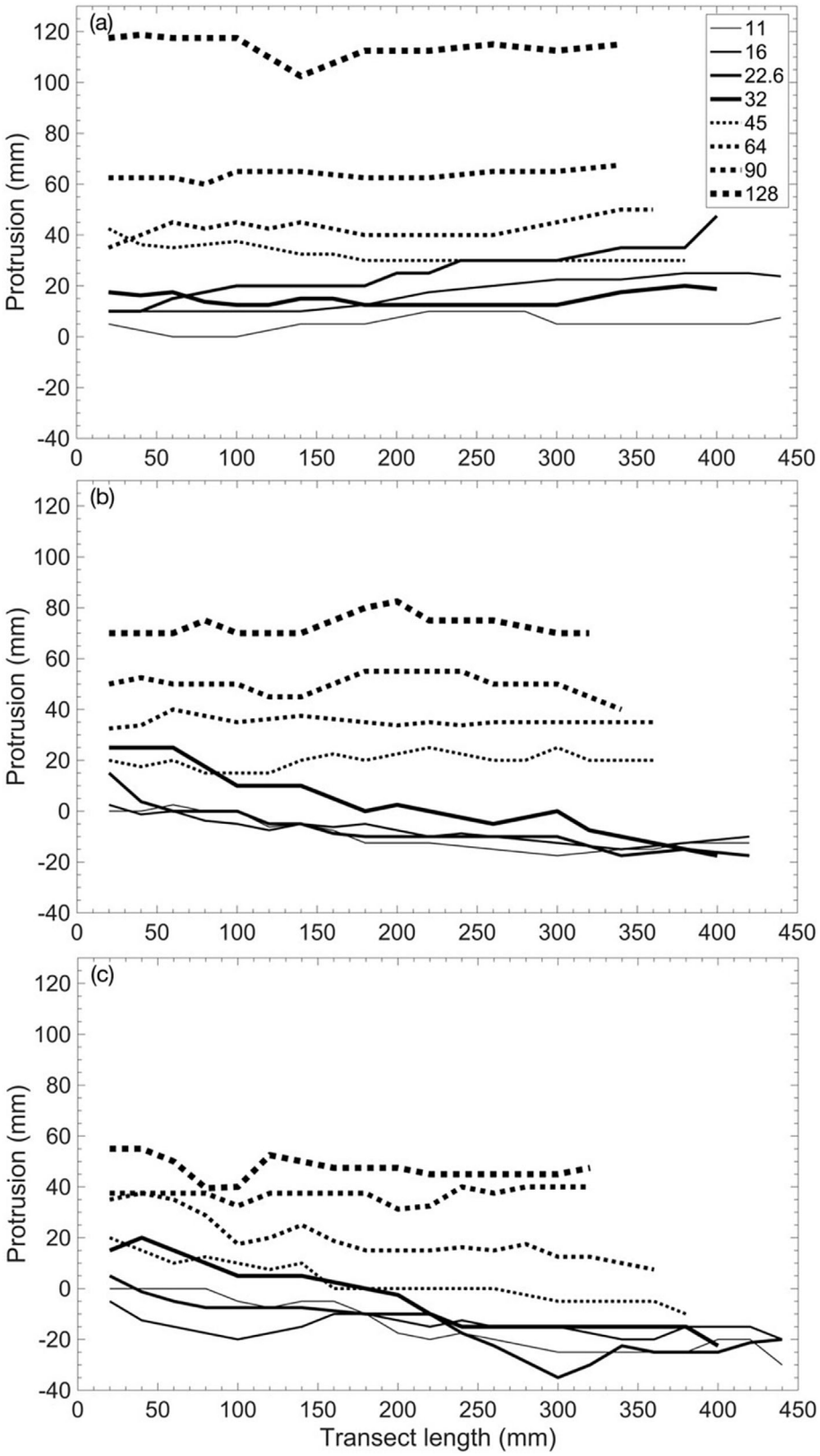

FIGURE 1 Median grain protrusion with increasing transect length for all grain sizes (11 to 128 mm) on (a) gravel ($D_{50} = 20$ mm), (b) cobble-gravel ($D_{50} = 50$ mm) and (c) gravel-cobble ($D_{50} = 57$ mm) patches. Each line is the median protrusion of multiple transects for a given D_i computed for progressively longer transects.

3.3 | The influence of GSD on hiding functions

We now explore if the underlying patch GSD affects hiding functions and the influence of uncertainties in the variables used to construct hiding functions. Regardless of the method used (fully populated vs. all mobile patches), τ^*_{c50} values (coefficient of hiding function) were similar between cG and gC patches but were much higher for G patches and had an intermediate value when all patches were combined (Figure 4a,b). We found that τ^*_{c50} did not systematically vary with patch sorting ($\sigma = \sqrt{D_{84}/D_{16}}$,), where σ was 2.03, 2.90, and 2.01 for the G, cG and gC patches, respectively.

The higher τ^*_{c50} on the G patches compared to the gC and cG patches (Figure 4a,b) was an unexpected result given that previous studies have documented that finer patches are either more mobile than, or are equally mobile as, coarse patches (e.g., Dietrich et al., 2005; Hodge et al., 2013; Lisle, 1995; Scheingross et al., 2013;

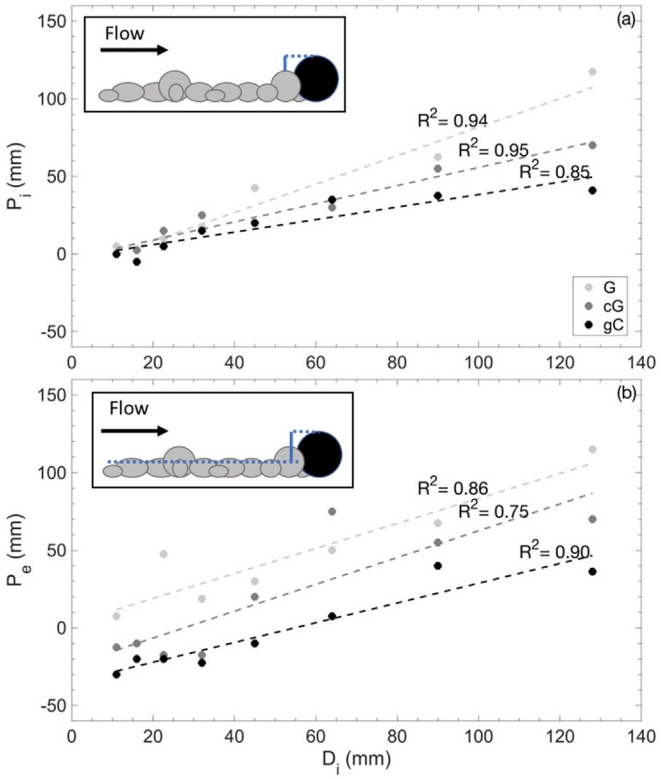

FIGURE 2 Measured median protrusion for each grain size (D_i) in each patch class (gravel (G), cobble-gravel (cG) and gravel-cobble (gC)). For each grain, protrusions were measured (a) immediately upstream (P_i), and (b) extended (P_e) upstream of the grain. A cartoon in each respective figure demonstrates the definitions of P_i and P_e where the grain of interest is shown in black.

Vericat et al., 2008; Yager et al., 2012a). In addition, τ^*_{c50} (~0.4) for the G patches was larger than the normally reported range of values even in steep channels (e.g., Lamb et al., 2008). Thus, we assumed that the hiding function for the G patches may have errors in its calculation and tested three possible alternative explanations for these high τ^*_{c50}. One potential explanation for high τ^*_{c50} in G patches is that the shear stresses acting on these patches were large enough to move the maximum installed grain size even at relatively low flows. This implies that τ^*_{c50} were overestimated because the applied shear stress at higher flows could have moved larger grain sizes than were installed as tracers. The largest grain size installed in G patches was not mobile until the largest observed discharge of 2.1 m^3/s and a low number of tracers moved in all events relative to the number of tracers that were installed (Table 1), which implies that high τ^*_{c50} cannot be explained through this mechanism. An alternate explanation for high τ^*_{c50} in G patches is the uncertainty in the mobile D_{84} in most events given the relatively low number of mobile tracers in this patch class (Table 1). We analysed potential errors in mobile D_i by using the largest grain size present on G patches as the mobile D_i in the hiding function. The largest possible mobile D_i would decrease τ^*_{c50}, which will determine if our mobile D_i possibly had errors that would put τ^*_{c50} within the range of those for the other patch classes. We obtained a minimum possible value of $\tau^*_{c50} = 0.09$, but no hiding function could be determined because D_i/D_{50} was constant in this calculation for all flows. Only when the mobile D_i was increased to the maximum grain size present on G patches, could we observe τ^*_{c50} in the range of that for cG and gC patches. However, again, we did not observe motion for such large grains in low flows, and this cannot be the explanation for high τ^*_{c50} for G patches.

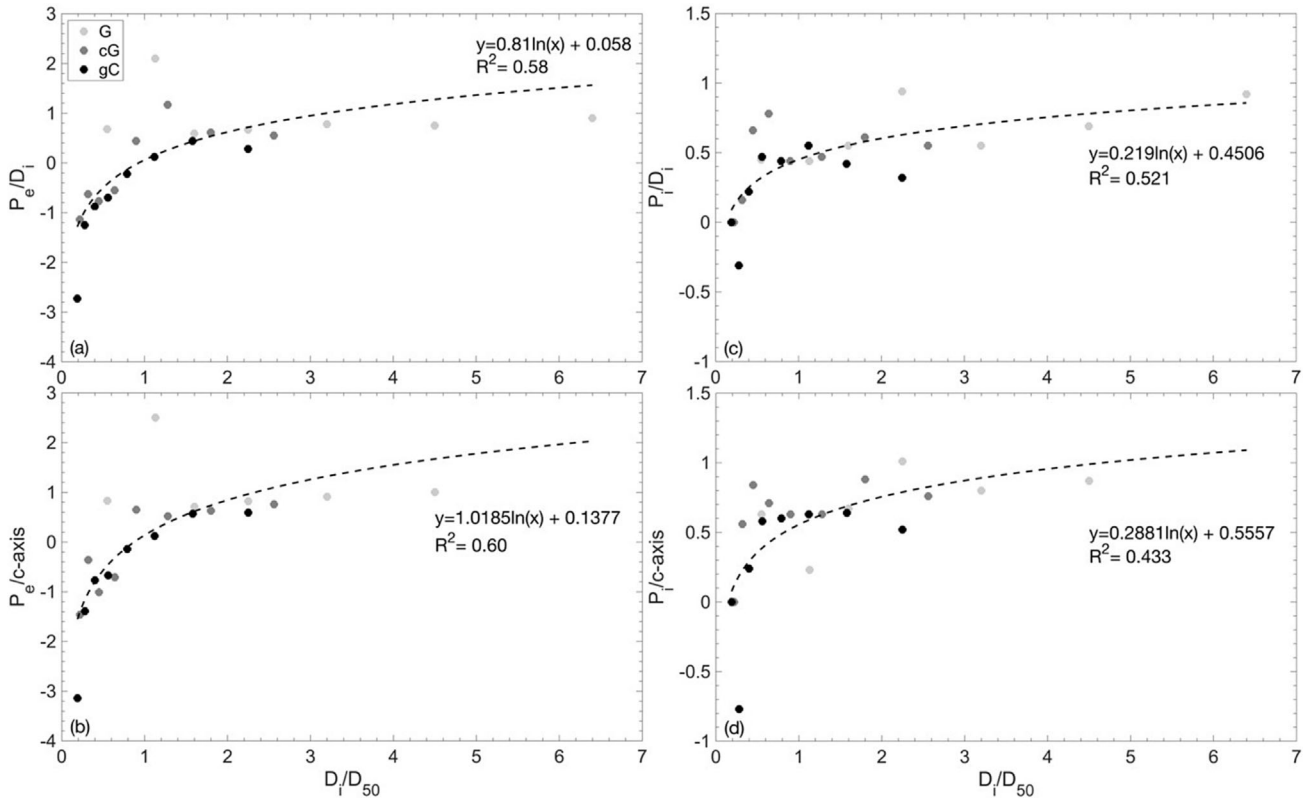

FIGURE 3 Protrusion (P) normalized with grain size (D_i) and grain *c*-axes for extended (a and b) and immediate upstream (c and d) protrusion scales for all patch classes. Each patch class is shown with a different coloured symbol.

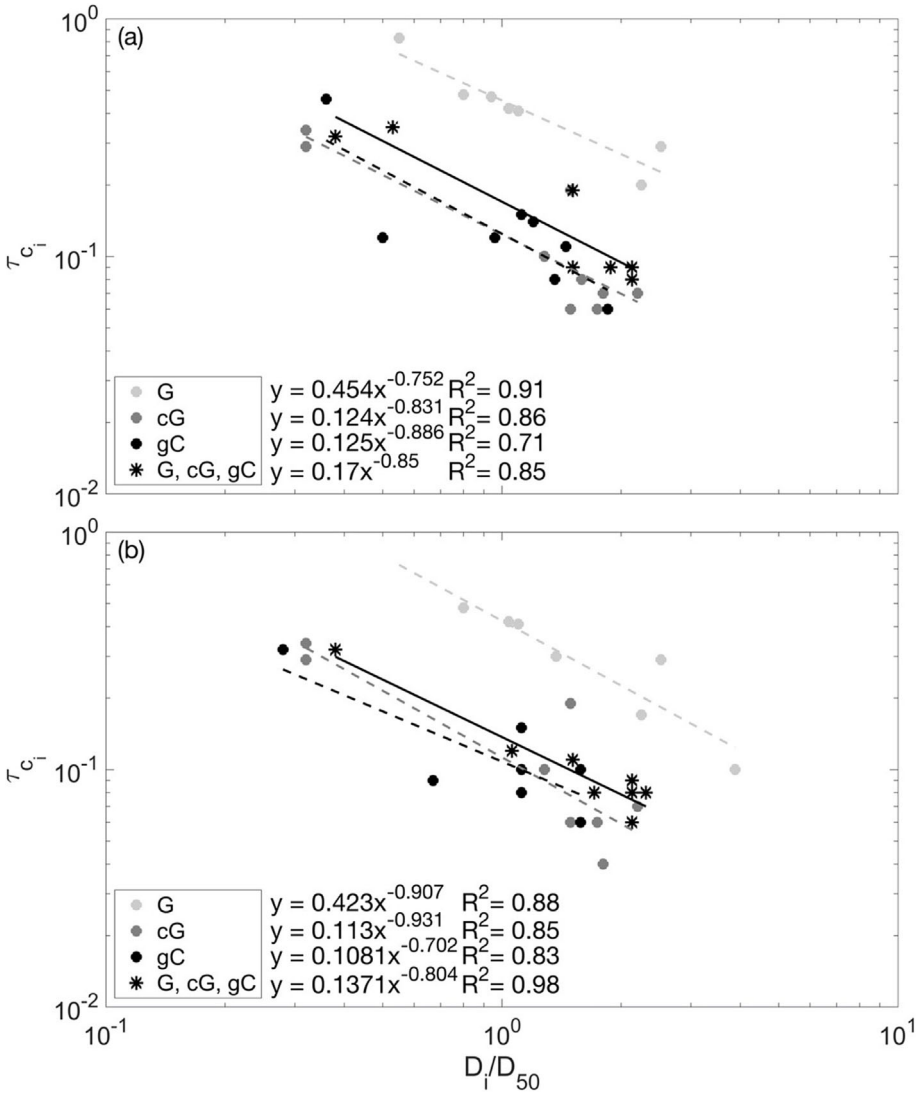

FIGURE 4 Hiding functions for each patch class and for all patch classes combined (different symbols). Hiding functions included mobile tracers and shear stresses (a) only on fully populated patches and (b) for all patches with mobile tracers.

A third explanation for the high τ^*_{c50} in G patches is that the 2D model could have calculated incorrectly high velocities and shear stresses on many of the G patches. The gravel patches with mobile tracers were often immediately downstream of boulders where the modeled 2D estimates of flow will likely have large errors because of plunging flow over boulders and flow recirculation downstream of the boulders (Monsalve et al., 2016). To explore if the modeled shear stresses in G patches could be incorrect, we compared the median shear stresses for each patch class using (1) all patches with mobile tracers, which was used for hiding functions in Figure 4b, (2) all fully populated patches with mobile tracers, which was used for hiding functions in Figure 4a and (3) all submerged patches regardless of whether they had installed or mobile tracers (Figure 5), which was not previously used in hiding functions. For a given flow discharge, the median shear stresses for all mobile and fully populated G patches (Figure 5a,b, respectively) were much higher than those for all submerged G patches (Figure 5c). This implies that the G patches with mobile tracers may have not been representative of all submerged G patches and could have artificially high shear stresses because the 2D model may not have accounted for highly 3D flow in these specific locations. For each of the cG and gC patch classes, these three different median shear stress estimates were largely in the same range of values for a given discharge (Figure 5), implying that the cG and gC patches with mobile tracers were representative of all submerged patches of these types.

We used the median shear stresses for all submerged G patches in the G patch hiding function calculation to test whether incorrect shear stresses on mobile G patches could explain the high τ^*_{c50} of G patches. Now, the G patch τ^*_{c50} was similar to that for the cG and gC patches (Figure 5d), which implies that the G patches could have similar hiding functions as the other patches if shear stresses on the G patches with mobile tracers were approximated using shear stresses from all G patches.

4 | DISCUSSION

4.1 | Protrusion variation with transect distance

We investigated if the upstream measurement distance would influence grain protrusion because different upstream sheltering lengths are often concurrently present and control the flow field at the particle scale. Various protrusion measurement scales have been explored such as immediate upstream topography (smallest distance scale) (Wiberg & Smith, 1987) and a distance of D_{84} (based on the surrounding GSD) upstream and downstream of a grain (intermediate distance

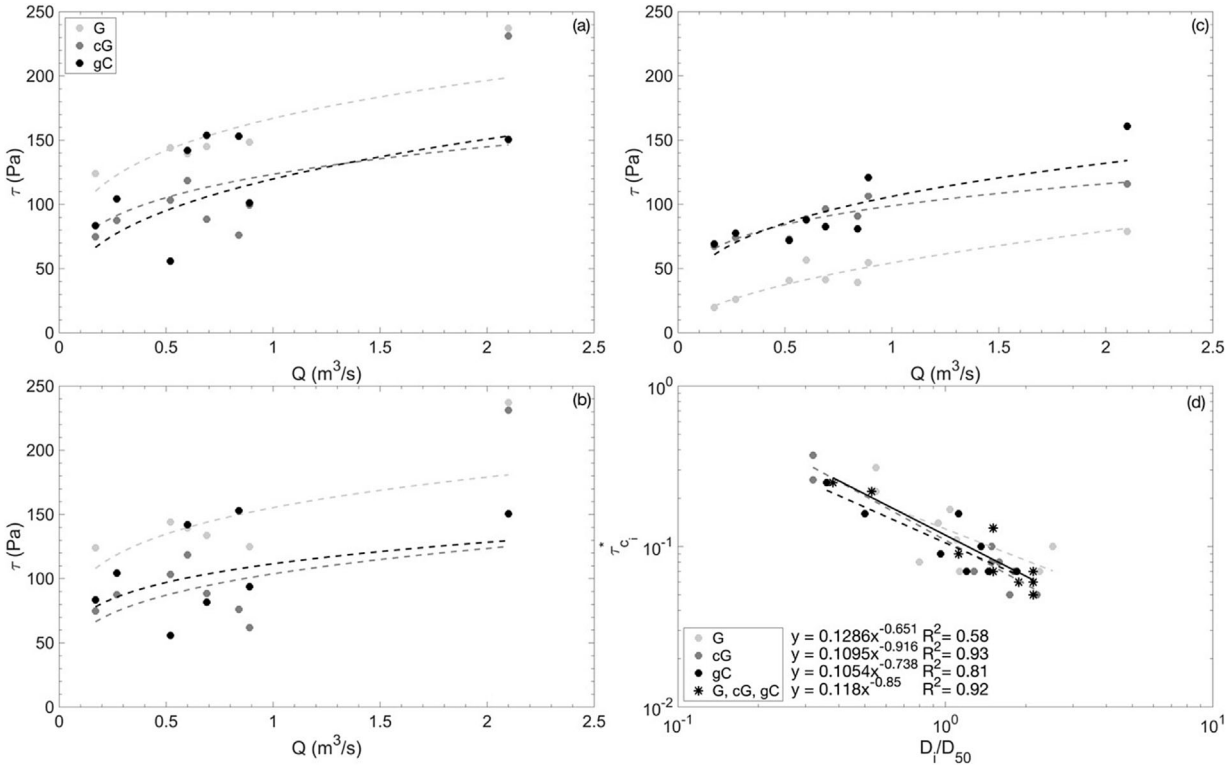

FIGURE 5 Median shear stresses for each peak discharge and each patch class on (a) only fully populated patches, (b) all patches with mobile tracers and (c) all submerged patches. Hiding functions (d) using shear stress on all submerged G, cG and gC patches.

scale) (Hodge et al., 2013; Kirchner et al., 1990). When considering the forces that are applied to a grain, upstream bed elevations beyond those immediately upstream of the grain (i.e., P_e) may be important. However, P_e can be potentially problematic as indicated by high measured protrusion values for the grain of interest (P_e/D_i and P_e/c-axis >2, Figure 3a,b). These high dimensionless protrusion values were the result of patch concavity, and falsely suggested that a grain protruded above the mean bed elevation by over 2 times the length of its *b*- or *c*-axis, which would not naturally occur.

Despite these potential issues with P_e, our protrusion estimates were mostly independent of transect length for grains larger than the patch median ($D_i > D_{50}$), which implies elevations immediately upstream of a grain may appropriately represent the upstream bed topography. The most relevant protrusion measurement for grains much smaller than the patch median size ($D_i < D_{50}$) is unknown because the median measured protrusion decreased with the incremental inclusion of more upstream measurements (Figure 1). Future work could investigate the relevant protrusion scale for these particles as well as the potential importance of larger protrusion scales. Larger protrusion scales could influence overall patch sheltering such as patch shape effects (flat, convex or concave), and for steep streams, the general elevation of an entire patch with respect to the nearest upstream boulder.

4.2 | Uncertainties in developed hiding functions

We registered grain displacements for all patch classes in which we installed tracer grains, and some tracers were found in other submerged patches or in new locations within the installation patch, which provided grain motions from natural placement. Of all 387 tracer motions, 40% (155 motions) were from fluvially placed locations. Although our $\tau^*_{c_{50}}$ from our final hiding functions are high (0.11–0.14, Figure 5d) compared to the typical range of values in lower gradient channels, (e.g., 0.03–0.086; Buffington & Montgomery, 1997), they are similar to values (~0.06 to 0.29) in other steep, natural streams (Buffington & Montgomery, 1997; Lamb et al., 2008; Mao et al., 2008; Mueller et al., 2005; Schneider et al., 2015; Yager et al., 2012a). This implies that including first grain motions did not result in low critical Shields stresses. In previous studies on steep channels, hiding function exponents (γ), which used a stress on the mobile fraction were −0.85 (Schneider et al., 2015), −0.16 (Yager et al., 2012a), −0.79 to −0.57 (Mao et al., 2008) and using a total shear stress were −0.62 (Yager et al., 2012a). Our γ values are within the range of values reported for lower gradient channels and are at the lower end of values for steep rivers.

Although both $\tau^*_{c_{50}}$ and γ were reasonable in our study, we did not expect that any of our $\tau^*_{c_{50}}$ values would be in the range reported for steep streams. High $\tau^*_{c_{50}}$ are usually related to steep reach-averaged bed slopes (Buffington & Montgomery, 1997; Bunte et al., 2013; Ferguson, 2012; Lamb et al., 2008; Prancevic & Lamb, 2015; Prancevic et al., 2014; Shvidchenko et al., 2001; Recking et al., 2009), because of the effects of large immobile boulders on the reach-averaged shear stress (Monsalve et al., 2016; Yager et al., 2012a), or arise from the effects of hydraulics specific to these channels (e.g., Lamb et al., 2008). For example, smaller $\tau^*_{c_{50}}$ that are within the typical range for lower gradient channels have also been reported for steep streams (Yager et al., 2012a). These lower $\tau^*_{c_{50}}$ values were estimated using an effective shear stress that only accounts

for the stress borne by mobile sediment and excludes the stress borne by immobile boulders (Nitsche et al., 2011; Schneider et al., 2015; Yager et al., 2012a).

Our $\tau^*_{c_{50}}$ have magnitudes similar to those that employ the total shear stress and were high compared to those that remove stresses borne by immobile boulders. This is surprising because we had indirectly accounted for the effects of large roughness elements in the bed topography used in the 2D model. Furthermore, our hiding function was developed on the same stream as studied by Schneider et al. (2015), who estimated $\tau^*_{c_{50}} = 0.19$ based on the total boundary shear stress, and Yager et al. (2012a), who used similar tracer grain methods and obtained $\tau^*_{c_{50}} = 0.07$. The differences in $\tau^*_{c_{50}}$ between our and these two studies must therefore be due to the method of calculating shear stresses used in the hiding functions (i.e., stress partitioning vs. 2D model). Our high $\tau^*_{c_{50}}$ may suggest that the 2D model may not always accurately depict the highly turbulent flow in 3D that occurs in the Erlenbach, and therefore may overestimate median shear stresses on some of the patches, as demonstrated for the G patches (see Figure 4). These results may alternatively suggest that stress-partitioning calculations may possibly over-estimate the stress borne by boulders, thereby producing relatively low $\tau^*_{c_{50}}$.

Regardless of the source of shear stress errors, our results indicate that $\tau^*_{c_{50}}$ strongly depends on the accuracy of the shear stresses employed in hiding functions. The reach-averaged shear stress is typically used to develop hiding functions and this may partly explain at least some of the wide variation in $\tau^*_{c_{50}}$ observed in the literature. The reach-averaged shear stress almost never occurs at the scale of an individual tracer particle motion or local bedload transport measurement, which are used to obtain the mobile grain sizes in hiding functions. Our results imply that obtaining accurate and representative shear stresses is important for developing and applying hiding functions. In lower gradient channels, 2D flow models may provide these accurate shear stresses better than the commonly used reach-averaged shear stresses. This is because lower gradient channels often have less flow complexity and therefore lower expected 2D model errors than will occur in the Erlenbach.

4.3 | Effects of GSD on patch-scale protrusion and hiding function equations

We investigated whether the underlying grain size distribution of each patch impacts the degree of size-selective entrainment (γ) and overall sediment mobility ($\tau^*_{c_{50}}$). Differences in all hiding function exponents were likely within methodological errors. For example, for any given patch class (gC, cG and G), the γ differences between our two grouping methods (all mobile patches vs. only populated patches) of 0.017–0.155 were about the same magnitudes as the γ differences of 0.154–0.229 between patch classes for a given method (Figure 4). Even when the hiding function for the G patch was corrected for improperly high shear stresses (Figure 5), γ still did not systematically vary with patch GSD. The $\tau^*_{c_{50}}$ for all final hiding functions (Figure 5) were similar between all patch classes and also did not vary with patch GSD. This implies that the effects of patch GSD on relative particle mobility are likely fully captured by using the normalized grain size (D_i/D_{50}) in hiding functions.

Similar hiding functions for all patch classes imply that different hiding functions may not be needed for individual patches and a single hiding function can be used to represent particle motion throughout the bed. This is important given the increasing use of bedload transport equations in 2D flow models to predict spatial variations in transport and local deposition and erosion. Our results imply that the hiding functions in bedload equations do not necessarily need to be adjusted to account for local patch GSD, which makes such 2D bedload modelling trackable. However, the variables that are used in hiding functions will likely need to be patch-specific because the onset of motion of a given grain size will depend on the underlying patch D_{50}. Therefore, patch-scale effects can control grain motion and patch D_{50} may need to be considered in reach-scale calculations of sediment transport. Finally, the bed grain size distributions for cG and gC patches were similar (see Monsalve et al., 2016, Figure 2) and these similarities could be partly responsible for the collapse of patch-scale hiding functions into one relation. Further work is needed to determine if these results would apply to a wide range of patch grain size distributions. In addition, our results are specifically for patches in the same channel and do not necessarily imply that two different reach-scale GSD should have the same hiding function.

Similar to the hiding function equations, we investigated whether the relations between dimensionless protrusion and dimensionless grain size varied with patch GSD. The median dimensionless protrusion (Figure 3) largely collapsed onto a single relation with D_i/D_{50} for all patch classes. This suggests that protrusion is dominantly controlled by the size of a grain relative to that of the underlying bed. Although patch specific effects (e.g., standard deviation of grain size distribution, grain sorting or patch topography) may contribute to scatter around the single logarithmic line, these effects do not seem to dominantly control protrusion in our data. Median protrusion may be estimated using the equation shown in Figure 3b combined with the measured D_{50} for each patch class. To estimate c axes, a grain shape would need to be assumed or the *c*-axis to be measured.

4.4 | Links between patches, protrusion, and relative particle mobility

Previous studies have demonstrated that the underlying reach-scale GSD may affect protrusion, but it is unclear if GSD at the patch scale affects protrusion. Conflicting results also exist as to whether the patch GSD influences the relative mobility of a grain of a particular size. Given that protrusion is a major control of the applied and resisting forces on individual grains, we would expect that if patch GSD affects protrusion, patch GSD should also influence relative particle mobility. We confirmed that patch GSD affects both protrusion and relative particle mobility through patch control on the relative grain size (D_i/D_{50}) of a given particle. Grains that had the same D_i/D_{50}, but that were located on different patches, generally had the same dimensionless median protrusion. Similarly, the same critical Shields stress occurred on different patch classes for the same D_i/D_{50} (Figure 5). In addition, our protrusion measurements demonstrated that regardless of the patch class, coarser grains emerge more from the bed surface than finer grains. This implies that hiding effects should be present on the bed, which is supported by our hiding function exponents between −0.65 and −0.92. Given that protrusion and

τ^*_{ci} are similarly modulated on patches through D_i/D_{50}, we conclude that protrusion is a dominant grain-scale variable controlling τ^*_{ci}, which has also been suggested by previous studies (Hodge et al., 2020; Yager et al., 2018). Other variables not being considered in this study may also affect hiding functions. Pivot angle could be primarily impacted by patch GSD through D_i/D_{50} as shown by Buffington et al. (1991) and Kirchner et al. (1990), but recent studies suggest that the effects of pivot angle on the critical Shields stress may be minimal (Hodge et al., 2020). Surface grains with greater intergranular friction (Buxton et al., 2015; Cúñez et al., 2022; Hodge et al., 2013; Yager et al., 2018) would likely have higher associated τ^*_{ci}, and this could vary between patch classes because of different amounts of fine sediment, different degrees of imbrication, or different porosities.

The single relations of dimensionless protrusion and τ^*_{ci} with D_i/D_{50} for all patch classes importantly also show how the underlying patch GSD affects the mobility of a given grain size. A given D_i will have different τ^*_{ci} between patch classes because of the different D_{50} used in D_i/D_{50} and the hiding function. Specifically, a given grain size will generally have a lower dimensional critical shear stress, and will be less mobile, on a coarser patch than a finer patch. This is likely mechanistically driven because a given D_i has a lower dimensional protrusion (Figure 2) on a coarser patch than a finer patch. These results support previous literature (Lisle et al., 1995; Vericat et al., 2008; Scheingross et al., 2013) that demonstrates particles are more readily mobile on finer than coarse patches.

Finally, our hiding function exponents further demonstrate that grain weight effects are important on patches because size-selective entrainment occurs on each patch class, despite patches having narrower GSDs than the entire bed. Although finer particles were more mobile than coarse grains on each patch, hiding effects made finer particles relatively less mobile than expected by their weight alone. Our hiding functions only include grain sizes that were less than, or similar to, the median grain size of the patch. Similar to our study, most studies report hiding functions with relative grain sizes concentrated in the finer grain fractions ($D_i/D_{50} < 2$) (e.g., Mao et al., 2008; Parker, 1990, 2008; Parker et al., 1982; Yager et al., 2012a). When coarser grains ($D_i/D_{50} > 3$) are a large component of hiding functions, hiding function exponents can be closer to −0.33 (Wilcock & Crowe, 2003). This suggests that weight effects may become more important than hiding effects (e.g., protrusion) for the coarser fractions on the bed. Although we did not measure motion of these coarser grains, our measured dimensionless protrusion increased with relative grain size for smaller grain sizes but remained almost constant for D_i/D_{50} larger than about 2 (Figure 3). This may provide a physical explanation for why coarser grain weight effects can dominate over hiding effects; once particles become very large, their relative protrusion no longer increases to offset their greater weights. Further research into hiding functions on patches that includes motion of these coarser grain sizes would help determine the relative importance of hiding and grain weight effects.

5 | CONCLUSION

We investigated the influence of patch-scale GSD on particle protrusion and grain mobility. Our results imply that grain size distributions in patches affect the relative mobility of a given grain size but not the degree of size-selective transport of different grain sizes. Hiding functions for different patch classes roughly collapsed onto a single line, suggesting that the relative underlying grain size (D_{50}) determines the mobility of a grain, but that all grain sizes experience size selective transport. Different hiding functions may not be needed to describe particle motion on different patch classes. For all patch classes, a single relation also existed between relative grain size (D_i/D_{50}) and median dimensionless protrusion, which can mechanistically explain why we obtained a similar hiding function for all patch types. However, for a given grain size, protrusion was higher and critical dimensional shear stresses were lower on finer patches. This demonstrates that sediment on finer patches may move at lower flows than the same grain sizes on coarse patches. For grains coarser than the median grain size, the distance over which protrusion was measured did not significantly impact our results but for finer grains, the scale of protrusion measurements can cause large differences in the median protrusion for a given grain size. To understand the grain scale mechanisms involved in the onset of sediment motion, further research is needed that focuses on near-bed flow velocities that interact with grains with a range of protrusion scales.

ACKNOWLEDGEMENTS

Funding for this research was provided by a National Science Foundation Career award to E.M. Yager (0847799), the Chilean National Agency for Research and Development – ANID though the programme FONDECYT Iniciación grant 11200949, and the Swiss Federal Research Institute WSL. Invaluable field assistance was provided by Alex Beer and Dani Merriman. Please contact Angel Monsalve (angelm@uidaho.edu) for the topographic, sediment grain size distributions, or hydraulic data. If you are interested in the Swiss bed load data, please contact Dieter Rickenmann (dieter.rickenmann@wsl.ch).

DATA AVAILABILITY STATEMENT

The data that support the findings of this study are available from the corresponding author upon reasonable request.

ORCID

Heidi E. J. Smith https://orcid.org/0000-0001-6808-451X
Jens M. Turowski https://orcid.org/0000-0003-1558-0565
Dieter Rickenmann https://orcid.org/0000-0002-2205-892X

REFERENCES

Barton, G.J., McDonald, R.R., Nelson, J.M. & Dinehart, R.R. (2005) Simulation of Flow and Sediment Mobility Using a Multidimensional Flow Model for the White Sturgeon Critical-Habitat Reach, Kootenai River near Bonners Ferry, Idaho: U.S. Geological Survey Scientific Investigations Report 2005-5230, 54 P.

Bathurst, J.C. (1987) Critical conditions for bed material movement in steep, boulder-bed streams. *International Association of Hydrological Sciences Publication*, 165, 309–318.

Beer, A.R., Turowski, J.M., Fritschi, B. & Rieke-Zapp, D.H. (2015) Field instrumentation for high-resolution parallel monitoring of bedrock erosion and bedload transport. *Earth Surface Processes and Landforms*, 40(4), 530–541. Available from: https://doi.org/10.1002/esp.3652

Beheshti, A.A. & Ataie-Ashtiani, B. (2008) Analysis of threshold and incipient conditions for sediment movement. *Coastal Engineering*, 55(5), 423–430. Available from: https://doi.org/10.1016/j.coastaleng.2008.01.003

Buffington, J.M., Dietrich, W.E. & Kirchner, J.W. (1992) Friction angle measurements on a naturally formed gravel streambed: implications for critical boundary shear stress. *Water Resources Research*, 28(2), 411–425. Available from: https://doi.org/10.1029/91WR02529

Buffington, J.M. & Montgomery, D.R. (1997) A systematic study of eight decades of incipient motion studies, with special reference to gravel-bedded rivers. *Water Resources Research*, 33(8), 1993–2029. Available from: https://doi.org/10.1029/97WR03138

Buffington, J.M. & Montgomery, D.R. (1999) A procedure for classifying textural facies in gravel-bed rivers. *Water Resources Research*, 35(6), 1903–1914. Available from: https://doi.org/10.1029/1999WR900041

Bunte, K., Abt, S.R., Swingle, K.W., Cenderelli, D.A. & Schneider, J.M. (2013) Critical Shields values in coarse-bedded steep streams. *Water Resources Research*, 49(11), 7427–7447. Available from: https://doi.org/10.1002/2012WR012672

Burtin, A., Hovius, N. & Turowski, J.M. (2016) Seismic monitoring of torrential and fluvial processes. *Earth Surface Dynamics*, 4(2), 285–307. Available from: https://doi.org/10.5194/esurf-4-285-2016

Buxton, T.H., Buffington, J.M., Yager, E.M., Hassan, M.A. & Fremier, A.K. (2015) The relative stability of salmon redds and unspawned streambeds. *Water Resources Research*, 51(8), 6074–6092. Available from: https://doi.org/10.1002/2015WR016908

Clayton, J.A. & Pitlick, J. (2007) Spatial and temporal variations in bed load transport intensity in a gravel bed river bend. *Water Resources Research*, 43(2), W02426. Available from: https://doi.org/10.1029/2006WR005253

Conner, J.T. & Tonina, D. (2014) Effect of cross-section interpolated bathymetry on 2D hydrodynamic model results in a large river. *Earth Surface Processes and Landforms*, 39(4), 463–475. Available from: https://doi.org/10.1002/esp.3458

Cúñez, F.D., Franklin, E.M., Houssais, M., Arratia, P. & Jerolmack, D.J. (2022) Strain hardening by sediment transport. *Phys. Rev. Research*, 4(2), L022055. Available from: https://doi.org/10.1103/PhysRevResearch.4.L022055

D'Agostino, V. & Lenzi, M.A. (1999) Bedload transport in the instrumented catchment of the Rio cordon: part II: analysis of the bedload rate. *Catena*, 36(3), 191–204. Available from: https://doi.org/10.1016/S0341-8162(99)00017-X

Dietrich, W.E., Nelson, P.A., Yager, E., Venditti, J.G., Lamb, M.P. & Collins, L. (2005) Sediment patches, sediment supply, and channel morphology. 79-90. In: Parker, G. & Garcia, M.H. (Eds.) *In 4th IAHR symposium on river coastal and estuarine Morphodynamics RCEM 2005*. Urbana, Illinois, USA: Taylor & Francis Group.

Diplas, P., Dancey, C.L., Celik, A.O., Valyrakis, M., Greer, K. & Akar, T. (2008) The role of impulse on the initiation of particle movement under turbulent flow conditions. *Science*, 322(5902), 717–720. Available from: https://doi.org/10.1126/science.1158954

Ferguson, R.I. (2012) River channel slope, flow resistance, and gravel entrainment thresholds. *Water Resources Research*, 48(5). Available from: https://doi.org/10.1029/2011WR010850

Hodge, R.A., Sear, D.A. & Leyland, J. (2013) Spatial variations in surface sediment structure in riffle–pool sequences: a preliminary test of the differential sediment entrainment hypothesis (DSEH). *Earth Surface Processes and Landforms*, 38(5), 449–465. Available from: https://doi.org/10.1002/esp.3290

Hodge, R.A., Voepel, H., Leyland, J., Sear, D.A. & Ahmed, S. (2020) X-ray computed tomography reveals that grain protrusion controls critical shear stress for entrainment of fluvial gravels. *Geology*, 48(2), 149–153. Available from: https://doi.org/10.1130/G46883.1

Houssais, M., Ortiz, C.P., Durian, D.J. & Jerolmack, D.J. (2015) Onset of sediment transport is a continuous transition driven by fluid shear and granular creep. *Nature Communications*, 6(1), 6527. Available from: https://doi.org/10.1038/ncomms7527

Katz, S.B., Segura, C. & Warren, D.R. (2018) The influence of channel bed disturbance on benthic chlorophyll a: A high resolution perspective. *Geomorphology*, 305, 141–153. Available from: https://doi.org/10.1016/j.geomorph.2017.11.010

Kirchner, J.W., Dietrich, W.E., Iseya, F. & Ikeda, H. (1990) The variability of critical shear stress, friction angle, and grain protrusion in water-worked sediments. *Sedimentology*, 37(4), 647–672. Available from: https://doi.org/10.1111/j.1365-3091.1990.tb00627.x

Lamarre, H., MacVicar, B. & Roy, A.G. (2005) Using passive integrated transponder (PIT) tags to investigate sediment transport in gravel-bed rivers. *Journal of Sedimentary Research*, 75(4), 736–741. Available from: https://doi.org/10.2110/jsr.2005.059

Lamb, M.P., Dietrich, W.E. & Venditti, J.G. (2008) Is the critical Shields stress for incipient sediment motion dependent on channel-bed slope? *Journal of Geophysical Research: Earth Surface*, 113(F2), F02008. Available from: https://doi.org/10.1029/2007JF000831

Lee, H. & Balachandar, S. (2012) Critical shear stress for incipient motion of a particle on a rough bed. *Journal of Geophysical Research: Earth Surface*, 117(F1), F01026. Available from: https://doi.org/10.11029/2011JF002208

Lisle, T.E. (1995) Effects of coarse woody debris and its removal on a channel affected by the 1980 eruption of Mount St. Helens, Washington. *Water Resources Research*, 31(7), 1797–1808. Available from: https://doi.org/10.1029/95WR00734

Lisle, T.E., Nelson, J.M., Pitlick, J., Madej, M.A. & Barkett, B.L. (2000) Variability of bed mobility in natural, gravel-bed channels and adjustments to sediment load at local and reach scales. *Water Resources Research*, 36(12), 3743–3755. Available from: https://doi.org/10.1029/2000WR900238

Malakoff, D. (2004) The river doctor. *Science*, 305(5686), 937–939. Available from: https://doi.org/10.1126/science.305.5686.937

Mao, L., Uyttendaele, G.P., Iroumé, A. & Lenzi, M.A. (2008) Field based analysis of sediment entrainment in two high gradient streams located in Alpine and Andine environments. *Geomorphology*, 93(3–4), 368–383. Available from: https://doi.org/10.1016/j.geomorph.2007.03.008

Masteller, C.C. & Finnegan, N.J. (2017) Interplay between grain protrusion and sediment entrainment in an experimental flume. *Journal of Geophysical Research - Earth Surface*, 122(1), 274–289. Available from: https://doi.org/10.1002/2016JF003943

Masteller, C.C., Finnegan, N.J., Turowski, J.M., Yager, E.M. & Rickenmann, D. (2018) History-dependent threshold for motion revealed by continuous bedload. *Geophysical Research Letters*, 2(46), 2583–2591. Available from: https://doi.org/10.1029/2018GL081325

Maturana, O., Tonina, D., McKean, J.A., Buffington, J.M., Luce, C.H. & Caamaño, D. (2014) Modeling the effects of pulsed versus chronic sand inputs on salmonid spawning habitat in a low-gradient gravel-bed river. *Earth Surface Processes and Landforms*, 39(7), 877–889. Available from: https://doi.org/10.1002/esp.3491

McDonald, R.R., Nelson, J.M., Kinzel, P.J. & Conaway, J.S. (2005) Modeling surface-water flow and sediment mobility with the multi-dimensional surface water modeling system (MD_SWMS). *US Geological Survey Fact Sheet*, 3078(6), 6.

Miller, A.J. & Cluer, B.L. (1998) Modeling Considerations for Simulation of Flow in Bedrock Channels. In: Tinkler, K.J. & Wohl, E.E. (Eds.) *Rivers over rock: fluvial processes in bedrock channels*, *Geophysical Monograph Series*, vol. 107. Washington, D.C.: American Geophysical Union, pp. 61–104. Available from: https://doi.org/10.1029/GM107p0061.

Molnar, P., Densmore, A.L., McArdell, B.W., Turowski, J.M. & Burlando, P. (2010) Analysis of changes in the step-pool morphology and channel profile of a steep mountain stream following a large flood. *Geomorphology*, 124(1–2), 85–94. Available from: https://doi.org/10.1016/j.geomorph.2010.08.014

Monsalve, A., Segura, C., Hucke, N. & Katz, S. (2020) A bed load transport equation based on the spatial distribution of shear stress – Oak Creek revisited. *Earth Surf. Dynam.*, 8(3), 825–839. Available from: https://doi.org/10.5194/esurf-8-825-2020

Monsalve, A., Yager, E.M., Turowski, J.M. & Rickenmann, D. (2016) A probabilistic formulation of bed load transport to include spatial variability of flow and surface grain size distributions. *Water Resources Research*, 52(5), 3579–3598. Available from: https://doi.org/10.1002/2015WR017694

Mueller, E.R., Pitlick, J. & Nelson, J.M. (2005) Variation in the reference Shields stress for bed load transport in gravel-bed streams and rivers.

Water Resources Research, 41(4), W04006. Available from: https://doi.org/10.1029/2004WR003692.

Mueller, E.R. & Pitlick, J. (2014) Sediment supply and channel morphology in mountain river systems: 2. Single thread to braided transitions. *Journal of Geophysical Research: Earth Surface*, 119(7), 1516–1541. Available from: https://doi.org/10.1002/2013JF003045

Nelson, J.M., Bennett, J.P. & Wiele, S.M. (2003) Flow and sediment-transport modeling. *Tools in Fluvial Geomorphology*, 18, 539–576. Available from: https://doi.org/10.1002/0470868333.ch18

Nelson, J.M. & McDonald, R.R. (1996) Mechanics and modeling of flow and bed evolution in lateral separation eddies. U.S. Geological Survey, Glen Canyon Environmental Studies Report, Flagstaff, Arizona, USA.

Nelson, J.M. & Smith, J.D. (1989) Evolution and stability of erodible channel beds. In: River meandering, *Water Resources Monograph*, vol. 12. Washington, D.C.: American Geophysical Union, pp. 321–377.

Nelson, P.A., Dietrich, W.E. & Venditti, J.G. (2010) Bed topography and the development of forced bed surface patches. *Journal of Geophysical Research: Earth Surface*, 115(F4), F04024. Available from: https://doi.org/10.1029/2010JF001747

Nitsche, M., Rickenmann, D., Kirchner, J.W., Turowski, J.M. & Badoux, A. (2012) Macroroughness and variations in reach-averaged flow resistance in steep mountain streams. *Water Resources Research*, 48(12), W12518. Available from: https://doi.org/10.1029/2012WR012091

Nitsche, M., Rickenmann, D., Turowski, J.M., Badoux, A. & Kirchner, J.W. (2011) Evaluation of bedload transport predictions using flow resistance equations to account for macro-roughness in steep mountain streams. *Water Resources Research*, 47(8), W08513. Available from: https://doi.org/10.1029/2011WR010645

Olinde, L. & Johnson, J.P.L. (2015) Using RFID and accelerometer-embedded tracers to measure probabilities of bed load transport, step lengths, and rest times in a mountain stream. *Water Resources Research*, 51(9), 7572–7589. Available from: https://doi.org/10.1002/2014WR016120

Palmer, M.A., Bernhardt, E.S., Allan, J.D., Lake, P.S., Alexander, G., Brooks, S., et al. (2005) Standards for ecologically successful river restoration. *Journal of Applied Ecology*, 42(2), 208–217. Available from: https://doi.org/10.1111/j.1365-2664.2005.01004.x

Parker, G. (1990) Surface-based bedload transport relation for gravel rivers. *Journal of Hydraulic Research*, 28(4), 417–436. Available from: https://doi.org/10.1080/00221689009499058

Parker, G. (2008) Transport of Gravel and Sediment Mixtures. In: García, M.H. (Ed.) *Sedimentation engineering: processes, measurements, modeling, and practice*. Reston, VA: American Society of Civil Engineers, pp. 165–251. Available from: https://doi.org/10.1061/9780784408148.ch03

Parker, G., Klingeman, P.C. & McLean, D.G. (1982) Bedload and size distribution in paved gravel-bed streams. *Journal of the Hydraulics Division*, 108(4), 544–571. Available from: https://doi.org/10.1061/JYCEAJ.0005854

Prancevic, J.P. & Lamb, M.P. (2015) Particle friction angles in steep mountain channels. *Journal of Geophysical Research: Earth Surface*, 120(2), 242–259. Available from: https://doi.org/10.1002/2014JF003286

Prancevic, J.P., Lamb, M.P. & Fuller, B.M. (2014) Incipient sediment motion across the river to debris-flow transition. *Geology*, 42(3), 191–194. Available from: https://doi.org/10.1130/G34927.1

Rattray, M., Jr. & Mitsuda, E. (1974) Theoretical analysis of conditions in a salt wedge. *Estuarine and Coastal Marine Science*, 2(4), 375–394. Available from: https://doi.org/10.1016/0302-3524(74)90006-1

Recking, A., Bacchi, V., Naaim, M. & Frey, P. (2009) Antidunes on steep slopes. *Journal of Geophysical Research: Earth Surface*, 114(F4), F04025. Available from: https://doi.org/10.1029/2008JF001216

Rickenmann, D. (1997) Sediment transport in Swiss torrents. *Earth Surface Processes and Landforms*, 22(10), 937–951. Available from: https://doi.org/10.1002/(SICI)1096-9837(199710)22:10<937::AID-ESP786>3.0.CO;2-R

Rickenmann, D. & McArdell, B.W. (2007) Continuous measurement of sediment transport in the Erlenbach stream using piezoelectric bedload impact sensors. *Earth Surface Processes and Landforms*, 32(9), 1362–1378. Available from: https://doi.org/10.1002/esp.1478

Rickenmann, D., Turowski, J.M., Fritschi, B., Klaiber, A. & Ludwig, A. (2012) Bedload transport measurements at the Erlenbach stream with geophones and automated basket samplers. *Earth Surface Processes and Landforms*, 37(9), 1000–1011. Available from: https://doi.org/10.1002/esp.3225

Scheingross, J.S., Winchell, E.W., Lamb, M.P. & Dietrich, W.E. (2013) Influence of bed patchiness, slope, grain hiding, and form drag on gravel mobilization in very steep streams. *Journal of Geophysical Research: Earth Surface*, 118(2), 982–1001. Available from: https://doi.org/10.1002/jgrf.20067

Schmeeckle, M.W., Nelson, J.M. & Shreve, R.L. (2007) Forces on stationary particles in near-bed turbulent flows. *Journal of Geophysical Research: Earth Surface*, 112(F2), F02003. Available from: https://doi.org/10.1029/2006JF000536

Schneider, J., Hegglin, R., Meier, S., Turowski, J.M., Nitsche, M. & Rickenmann, D. (2014) Studying sediment transport in mountain rivers by mobile and stationary RFID antennas. *River Flow*, 2010, 1723–1730.

Schneider, J.M., Rickenmann, D., Turowski, J.M., Bunte, K. & Kirchner, J.W. (2015) Applicability of bed load transport models for mixed-size sediments in steep streams considering macro-roughness. *Water Resources Research*, 51(7), 5260–5283. Available from: https://doi.org/10.1002/2014WR016417

Segura, C. & Pitlick, J. (2015) Coupling fluvial-hydraulic models to predict gravel transport in spatially variable flows. *Journal of Geophysical Research: Earth Surface*, 120(5), 834–855. Available from: https://doi.org/10.1002/2014JF003302

Shields, A. (1936) Anwendung der Ähnlichkeitsmechanik auf die Geschiebebewegung: Berlin, Preussische Versuchanstalt für Wasserbau und Schiffbau. Mitteilungen, no. 26, 25 p. Ph.D. Thesis. Technical University Berlin.

Shvidchenko, A.B., Pender, G. & Hoey, T.B. (2001) Critical shear stress for incipient motion of sand/gravel streambeds. *Water Resources Research*, 37(8), 2273–2283. Available from: https://doi.org/10.1029/2000WR000036

Skidmore, P.B., Shields, F.D., Doyle, M.W. & Miller, D.E. (2001) A Categorization of approaches to natural channel design. In: Hayes, D.F. (Ed.) *Proceedings of the 2001 wetlands engineering and river restoration conference*. Reston, VA: American Society of Civil Engineers, pp. 429–440. Available from: https://doi.org/10.1061/40581(2001)38

Turowski, J.M., Badoux, A., Leuzinger, J. & Hegglin, R. (2013) Large floods, alluvial overprint, and bedrock erosion. *Earth Surface Processes and Landforms*, 38(9), 947–958. Available from: https://doi.org/10.1002/esp.3341

Turowski, J.M., Yager, E.M., Badoux, A., Rickenmann, D. & Molnar, P. (2009) The impact of exceptional events on erosion, bedload transport and channel stability in a step-pool channel. *Earth Surface Processes and Landforms*, 34(12), 1661–1673. Available from: https://doi.org/10.1002/esp.1855

Vericat, D., Batalla, R.J. & Gibbins, C.N. (2008) Sediment entrainment and depletion from patches of fine material in a gravel-bed river. *Water Resources Research*, 44(11), W11415. Available from: https://doi.org/10.1029/2008WR007028

Voepel, H., Leyland, J., Hodge, R., Ahmed, S. & Sear, D. (2019) Development of a vector-based 3D grain entrainment model with application to X-ray computed tomography (XCT) scanned riverbed sediment. *Earth Surface Processes and Landforms*, 44(15), 3057–3077. Available from: https://doi.org/10.1002/esp.4608

Wiberg, P.L. & Smith, J.D. (1987) Calculations of the critical shear stress for motion of uniform and heterogeneous sediments. *Water Resources Research*, 23(8), 1471–1480. Available from: https://doi.org/10.1029/WR023i008p01471

Wilcock, P.R. & Crowe, J.C. (2003) Surface-based transport model for mixed-size sediment. *Journal of Hydraulic Engineering*, 129(2), 120–128. Available from: https://doi.org/10.1061/(ASCE)0733-9429(2003)129:2(120)

Wolman, M.G. (1954) A method of sampling coarse river-bed material. *Eos, Transactions American Geophysical Union*, 35(6), 951–956. Available from: https://doi.org/10.1029/TR035i006p00951

Wyss, C.R., Rickenmann, D., Fritschi, B., Turowski, J.M., Weitbrecht, V. & Boes, R.M. (2016) Measuring bed load transport rates by grain-size fraction using the swiss plate geophone signal at the erlenbach. *Journal of Hydraulic Engineering*, 142(5), 04016003. Available from: https://doi.org/10.1061/(ASCE)HY.1943-7900.0001090

Yager, E.M., Dietrich, W.E., Kirchner, J.W. & McArdell, B.W. (2012a) Patch dynamics and stability in steep, rough streams. *Journal of Geophysical Research: Earth Surface*, 117(F2), W07418. Available from: https://doi.org/10.1029/2011JF002253

Yager, E.M., Dietrich, W.E., Kirchner, J.W. & McArdell, B.W. (2012b) Prediction of sediment transport in step-pool channels. *Water Resources Research*, 48, W01541. Available from: https://doi.org/10.1029/2011WR10829

Yager, E.M., Schmeeckle, M.W. & Badoux, A. (2018) Resistance is not futile: grain resistance controls on observed critical Shields stress variations. *Journal of Geophysical Research: Earth Surface*, 123(12), 3308–3322. Available from: https://doi.org/10.1029/2018JF004817

Yager, E.M., Turowski, J.M., Rickenman, D. & McArdell, B.W. (2012) Sediment supply, grain protrusion, and bedload transport in mountain streams. *Geophysical Research Letters*, 39(10), L10402. Available from: https://doi.org/10.1029/2012GL051654

SUPPORTING INFORMATION

Additional supporting information can be found online in the Supporting Information section at the end of this article.

How to cite this article: Smith, H.E.J., Monsalve, A.D., Turowski, J.M., Rickenmann, D. & Yager, E.M. (2023) Controls of local grain size distribution, bed structure and flow conditions on sediment mobility. *Earth Surface Processes and Landforms*, 1–15. Available from: https://doi.org/10.1002/esp.5599